Corrosion Science 136 (2018) 231–243

Contents lists available at ScienceDirect

Corrosion Science

journal homepage: www.elsevier.com/locate/corsci

Corrosion behavior of WC-Co coatings deposited by cold gas spray onto AA 7075-T6

F.S. da Silva[a,b], N. Cinca[b], S. Dosta[b], I.G. Cano[b], M. Couto[b], J.M. Guilemany[b], A.V. Benedetti[a,*]

[a] São Paulo State University (UNESP), Institute of Chemistry, Rua Prof. Francisco Degni, 55, P.O. Box 355, 14800-060, Araraquara, SP, Brazil
[b] Barcelona University, CPT, Martí I Franqués 1, 08028 Barcelona, Spain

ARTICLE INFO

Keywords:
Cold spray
Metal coatings
EIS
Polarization
SEM
XRD

ABSTRACT

This work reports a morphological, mechanical, and corrosion resistance characterization of WC-12Co and WC-25Co coatings deposited by cold gas spray (CGS) onto AA 7075-T6 alloy. Cross-sectional images of the coatings revealed dense structures with low porosities. The coating thicknesses were 65 μm for WC-12Co and 118 μm for WC-25Co. XRD analysis showed that no fragile phases were formed in the coatings. SEM images and electrochemical results obtained after 700 h exposure to NaCl solution showed that WC-25Co exhibited better corrosion resistance performance. The WC-12Co and WC-25Co coatings withstood 1000 and 3000 h of salt fog spray test, respectively.

1. Introduction

Aluminum alloys such as AA 7075-T6 are widely used as structural components in aircraft manufacture, as well as in many other industries, due to their high strength/weight ratios [1,2]. Nevertheless, these alloys can be affected by various types of corrosion, such as pitting and galvanic corrosion, intergranular corrosion, stress cracking corrosion, and exfoliation corrosion [1–5].

It is well known that in chloride ion-containing solutions, AA 7075-T6 alloy is mainly susceptible to severe localized corrosion and intergranular corrosion, due to the presence of the elements Mg, Zn, and Cu, among others [1,2,6]. Localized corrosion usually initiates at heterogeneities of the microstructure of the alloy, such as coarse intermetallic phases, constituent particles, inclusions, and precipitates or segregations at grain boundaries. Among these, coarse intermetallic phases have especially attracted attention, because they are the most prominent initiation sites in alloys, due to galvanic coupling effects. It is well known that Cu-containing intermetallic phases are cathodic with respect to the matrix, so they promote the dissolution of the surrounding matrix [6]. Intermetallic phases rich in Mg or Zn are usually anodic with respect to the matrix, so they dissolve first. The localized corrosion can lead to sudden and unpredicted failures and deterioration of metal structures, hence increasing both costs and maintenance requirements. Protective WC-Co coatings have been used to protect Al alloys from localized and other forms of corrosion, as well as to improve wear resistance [7–12].

WC-Co coatings are composed of WC particles dispersed in a metallic Co matrix [7,9–13]. This type of coating exhibits the high temperature and abrasion resistance of ceramics and the ductility of metallic materials. Due to these properties, WC-Co coatings are widely used for applications where high mechanical performance and corrosion resistance are required, such as for the turbine blades of hydroelectric power plants, airplane landing gear, diesel engines, and rollers in paper industries [13–15].

WC-Co materials can be applied by the high velocity oxy-fuel (HVOF) method as coatings on steel [16–26] and aluminum alloys [7,8], as well as by the high velocity air-fuel (HVAF) method [27], plasma spraying [27–30], low pressure plasma spraying [27], and in the form of electrospark granules [31]. The resulting materials have been employed for various purposes when high resistance to abrasion, sliding, fretting, and erosion is required, with these properties depending on the density and particle size of the powder, spraying conditions, and the spray technique used [7,12,15,32]. These coatings have recently been used to obtain materials with low decarburization [22], to improve surface hardness [22,33] without developing brittle phases [34], to increase adhesion of the coating/substrate by thermal treatment or by adding a layer of different material on the substrate [30], to act as a barrier to avoid attack of a liquid metal on the substrate [34], to protect steel from water droplet erosion [35], and to increase wear resistance at temperatures up to 600 °C in air or higher temperatures in argon atmospheres [27,36].

These techniques use high temperatures during spraying, which can reach up to 3000 °C, leading to total or partial melting of the particles, and they can be accelerated by applying a compressed gas flow to the

* Corresponding author.
E-mail address: benedeti@iq.unesp.br (A.V. Benedetti).

https://doi.org/10.1016/j.corsci.2018.03.010
Received 30 June 2017; Received in revised form 6 March 2018; Accepted 7 March 2018
Available online 13 March 2018
0010-938X/

surface [7,12]. Problems associated with HVOF coatings are intrinsic characteristics of the process that can lead to the formation of pores and cracks, and chemical modification of the feedstock powder [7,12]. Cracks and residual stress mainly occur between the layers of deposited material, due to the fast solidification of sprayed particles, leading to the formation of a porous coating that allows the diffusion of electrolyte to the substrate, causing the initiation of corrosion. The use of high temperatures leads to changes in the phases of the feedstock material, due to its degradation and the formation of oxides and brittle phases, which can change the mechanical properties and corrosion resistance of coatings [13,7,12,37–39].

When WC-Co is deposited onto aluminum alloys using HVOF, formation of the coating can be hindered by the difference in thermal expansion coefficients of the coating and the substrate [7]. This difference leads to a residual stress that affects the mechanical stability of the coating and its corrosion performance. For these substrates, the contraction during cooling causes stresses and crack formation, not only between layers, but also at the substrate/coating interface, resulting in coating delamination [7]. Suggested ways to overcome this problem include the use of a substrate cooling system or resins applied to the substrate surface prior to the deposition [40–42]. Post-treatments and sealing coatings have been also investigated [43], but they make the process slower and more expensive.

Alternatively, cold gas spray (CGS) technology can be used to produce thicker WC-Co coatings that provide wear and corrosion resistance at lower cost [9–12,44,45] when applied to steel [9,45] and aluminum alloys [9–11]. In CGS, a solid powder is heated at low temperatures ($< 1000\,^{\circ}C$) and the particles are accelerated to between 500 and 1200 $m\,s^{-1}$ [9,11,45,46], depending on the gas used, spraying parameters, and nozzle design. When the velocity of the particles exceeds a certain critical value, the energy associated with the impact causes intense plastic deformation of the particle and the substrate [47]. The main reported bonding mechanism is by the occurrence of adiabatic shear stabilities (ASIs) which take place when particle softening overcomes its work hardening during the process [15,32,46]; in some case, the impact energy can even lead to melting at particle shells, resulting in strong bonds during coating formation [46]. Different to HVOF, the high kinetic energy and low thermal energy achieved during the CGS spraying process [48] act to reduce residual stresses, oxidation, and degradation of the feedstock material [46,49]. Therefore, these characteristics ensure that CGS can produce coatings using metallic-ceramic starting materials. Previous studies have investigated the production of cobalt-based coatings by CGS under various conditions, including spraying onto a variety of substrates, use of feedstock powders with different particle size, composition and morphology, and use of different spray parameters [10–12,45,50].

Evaluation has also been made of coatings sprayed onto different substrates using feedstock WC-Co powders with different Co contents [11,12,50]. Coatings formed from powders with higher amounts of Co showed greater deposition efficiencies and denser microstructures, since a higher binder content leads to greater plastic deformation of the particles and high effectiveness in interlocking among particles and between the particles and the substrate.

The effects of spraying parameters and particle size (nano- and micrometric) were investigated for the deposition of WC-Co coatings onto stainless steel [45]. Under optimized conditions, the coatings obtained from the nanometric powder showed hardness of 2053 HV and thickness up to 900 µm, while when micrometer particles were used, the hardness decreased to 918 HV and the thickness decreased to 200 µm [45].

Couto et al. [10,12] evaluated the microstructural and mechanical properties of WC-Co coatings on AA 7075-T6 alloy obtained using HVOF and CGS. The WC-25Co coatings obtained by the two techniques showed dense microstructures and thicknesses of 211 µm (CGS) and 163 µm (HVOF). The adhesion of the CGS coating (65 ± 4 MPa) was almost three times greater than that of the HVOF coating, while the hardness of both coatings was ~900 HV. XRD analysis of the coatings showed the presence of brittle phases such as W_2C, W, Co_6W_6C, and Co_3W_3C when the deposition was performed by HVOF. On the other hand, the CGS coating showed no change, compared to the starting material. The abrasive wear rate was $\sim 2 \times 10^{-5}\,mm^3\,Nm^{-1}$ for the two coatings, while in the sliding wear test, the HVOF coating lost five times more material, compared to the CGS coating.

In the present work, AA 7075-T6 alloy was used as substrate. This highly heterogeneous alloy is composed of an Al matrix, secondary phase particles (hardening precipitates, dispersoids, and constituent particles), and grain boundary (GB) regions with $Mg(ZnCuAl)_2$ particles in one side of the GB and a precipitate-free zone (PFZ) or a solute-depleted zone (SDZ) with depletion of Zn and Cu [51]. In chloride solutions, this alloy presents two breakdown potentials: the first, at more active potentials, is attributed to the dissolution of a very thin mechanically deformed surface layer; the second, at less negative potentials, is attributed to the formation of pits inside the matrix. The dissolution of a very thin layer, which was apparently a consequence of the mechanical polishing process, was demonstrated previously using an *in situ* observation system [51,52].

Characterization of the microstructure and mechanical behavior has shown that the WC-Co coatings obtained by CGS are promising substitutes for HVOF coatings; however, the corrosion performance of these coatings must be determined. Therefore, this work focused on investigation of the microstructure and corrosion resistance of WC-Co coatings produced by CGS with different feedstock powders (WC-12Co and WC-25Co) deposited onto AA 7075-T6.

2. Experimental

2.1. Feedstock materials, substrate, and reactants

The powders used were WC-Co cermets with 12 wt% and 25 wt% cobalt contents, obtained by agglomeration and sintering (Fujimi Inc., Kiyosu, Japan). Flat (50 mm × 20 mm × 5 mm) and cylindrical (∅ = 25.4 mm and h = 25.4 mm) coated and uncoated AA 7075-T6 alloy (0.18 wt% Cr, 1.2 wt% Cu, 2.1 wt% Mg, 5.1 wt% Zn, and balance Al) substrates were used in the electrochemical studies. The substrates were degreased with acetone and the surfaces were abraded with P240 SiC paper, resulting in a surface roughness (R_a) of ~1 µm. The electrolyte used was an aqueous 3.5 wt% NaCl (99.8%, Sigma-Aldrich) solution prepared with Milli-Q water (18.2 MΩ cm).

2.2. Coating preparation

The spraying of the WC-Co coatings was performed at the Thermal Spray Centre in Barcelona (Spain). A Kinetics 4000/17 kW system (Cold Gas Technology, Ampfing, Germany) was used at a maximum operating pressure of 40 bar, temperature of 800 °C, and with nitrogen as the carrier gas. A WC-based nozzle (D24) was used to deposit the coatings. Firstly, the CGS parameters were optimized to improve the deposition efficiency and adhesion. Evaluation was made of pressures from 20 to 40 bar, temperatures from 400 to 800 °C, and spray distances from 10 to 40 mm. Other parameters (gun transverse speed, feed rate, and spray angle) were kept constant. Previous experiments performed using low temperatures, pressures below 30 bar, and distances greater than 30 mm resulted in deposits with high porosity, poor cohesion between substrate and coating, delamination and the presence of cracks, and poor coating deposition efficiency. The following coatings were performed: WC-12Co was applied using a traversing velocity of 100 $mm\,s^{-1}$, P/T ratio of 0.037, and single-layer deposition; WC-25Co was applied using a traverse velocity of 250 $mm\,s^{-1}$, P/T ratio of 0.044, and four-layer deposition [9,11].

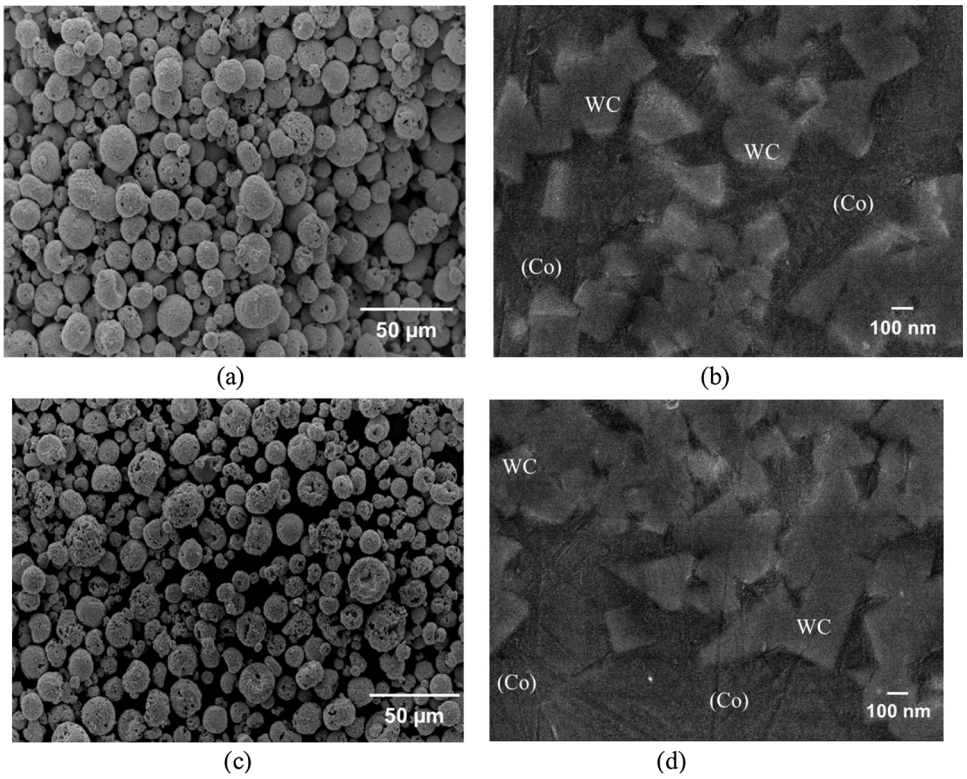

Fig. 1. SEM images of the feedstock powders: (a) free surface of the WC-12Co powder, (b) cross-section of the WC-12Co powder, (c) free surface of the WC-25Co powder, and (d) cross-section of the WC-25Co powder.

2.3. Structural, morphological, and chemical characterization

The powders and coatings were characterized by scanning electron microscopy (SEM) using a JEOL JSM-5310 microscope coupled to an X-ray microanalysis (EDS) system. The phase composition was analyzed by X-ray diffraction (XRD) using a Siemens Model D5000 diffractometer. The particle size distribution of the powders was analyzed by laser diffraction spectroscopy (LS). The coating thickness was determined from cross-sectional SEM images, using Image J software. The porosity of the coatings was estimated by analyzing the images using Image J software, according to the ASTM E2109-01 protocol (Standard Test Methods for Determining Area Percentage Porosity in Thermal Sprayed Coatings).

2.4. Mechanical characterization and hardness testing

Sliding wear tests were carried out using a ball-on-disk (BoD) method to determine the friction coefficients, following the ASTM G99-04 standard procedure. The tests were performed using a WC-6Co counterpart ball (11 mm diameter), a sample relative velocity of 131 rpm, a total testing distance of 1000 m, and a load force of 15 N for a diameter of 14 mm. The humidity and temperature were kept below 20% and 25 °C, respectively. The wear tracks produced on the coatings were studied using SEM and a Leica confocal laser system to measure the volume of material lost and to recreate the images of the wear tracks.

Vickers hardness tests were also performed on cross-sections of the WC-25Co coating and substrate, according to the ASTM E384-99 standard. The mean values were obtained from at least 15 indentations performed using loads of 100 gf for the substrate and 300 gf for the coatings, both applied for 15 s on polished cross-sections of the samples. The hardness test was not performed for the WC-12Co coating, because the conditions established in the ASTM E384-99 protocol were not satisfied and the low thickness of the coating would lead to a large error.

2.5. Corrosion studies

Electrochemical measurements were performed using a Gamry Reference 600 system, in aerated and unstirred 3.5% NaCl solution, at 25 ± 1 °C, with a conventional three-electrode Tait type cell [53]. The reference electrode was $Ag|AgCl|KCl_{3mol/L}$ coupled to a Luggin capillary, the auxiliary electrode was a Pt mesh, and the working electrode was the substrate or coated substrate, fixed at the bottom of the electrochemical cell. The specimen area exposed to the electrolyte solution was 1 cm^2. The corrosion resistances of the samples were evaluated by measurements using open circuit potential (E_{OCP}), linear polarization (R_p), potentiodynamic polarization, electrochemical impedance spectroscopy (EIS), and salt spray tests.

For short immersion times, the corrosion resistances of the samples were evaluated using open circuit potential during 18 h, followed by R_p with application of ± 10 mV *vs.* E_{OCP} and recording at 0.166 mV s^{-1}. For all samples, potentiodynamic polarization curves were also performed after 18 h of E_{OCP} measurements, however the anodic and cathodic branches were separately obtained, respectively, in the potential range from −0.050 to +0.300 V *vs.* E_{OCP} and from + 0.020 to −1.0 V *vs.* E_{OCP}, at 0.166 mV s^{-1}. For the WC-25Co sample, measurements were also made in the cathodic branch, in the absence of oxygen in the solution, in the potential range from +0.020 to −1.0 V *vs.* E_{OCP}, at 0.166 mV s^{-1}. The Stern-Geary equation was used to obtain the corresponding R_p values from i_{corr} and the Tafel plot slopes b_a and b_c.

EIS and E_{OCP} measurements were also performed for relatively long immersion times of 196 h for the AA 7075-T6 substrate, 600 h for WC-12Co, and 700 h for WC-25Co. EIS measurements for the coated samples were performed at 1 h and then every 24 h during the immersion, in the frequency range from 100 kHz to 5 mHz, using application of a sinusoidal potential perturbation of 10 mV rms on E_{OCP}, with 10 points/frequency decade. The experimental data were tested for consistency using the Kramers-Kronig transform (KKT), available in the Gamry system software, and compliance was obtained for all the experimental

EIS data for the coatings. The electrical equivalent circuit (EEC) obtained using Z-view® software was employed for quantitative analysis of the EIS responses.

Salt spray tests of the as-deposited WC-Co coatings were performed in neutral 5 wt% NaCl at 35 °C for 1000 h, in accordance with the ASTM B117-11 protocol. Since WC-25Co showed no corrosion signals up to 1000 h (the time established in the protocol), the salt spray test was continued up to a total time of 3000 h.

3. Results and discussion

3.1. Structural, morphological, and chemical characterizations

The LS analysis showed that both powders presented a particle size range from -26 + 8 μm, with a mean particle size of 15 ± 2 μm (Figs. 1Sa and 1Sb, Supplementary data, *SD*). SEM images of the free surfaces (Fig. 1a and c) showed that the two powders obtained from agglomeration and sintering processes were uniform, porous, and had similar spherical morphologies. SEM images of the powder cross-sections showed submicron WC particles randomly distributed in the matrices (Fig. 1b and d). EDS analysis (Fig. 2S, *SD*) showed that the particles were composed of WC, because the particle areas were rich in tungsten, while the other dark phase around the WC grains was cobalt, which acted as a binder.

The XRD patterns (Fig. 2) for the feedstock powders and the coatings showed the same characteristic peaks. WC and Co phases were observed, while W_2C, W, Co_6W_6C, and Co_3W_3C phases, normally formed when the material undergoes a high degree of oxidation or partial degradation, were absent. Therefore, there were no changes in the material compositions and the coatings obtained were homogeneous and almost oxide-free (as were the starting materials). Since CGS uses high kinetic energy and low thermal energy during the spraying process, the coatings formed are almost free of oxides, and chemical reactions that could lead to the formation of new phases do not occur [48,49,54].

Fig. 3 shows SEM images of the cross-sections and polished surfaces of the WC-Co coatings. SEM analysis of the cross-sections revealed typical microstructures of cold-sprayed coatings, with the particles being severely deformed and without the presence of metallic oxides, cracks, or interconnected porosity at the metal/coating interface or along the coating [55]. The top layers of the coatings were less compact than the bottom layers, in agreement with the literature [56], which describes CGS coatings as essentially consisting of a top layer with some porosity and a dense bottom layer. The porosities of the coatings were estimated to be 0.7 ± 0.1% for WC-12Co and 0.4 ± 0.1% for WC-25Co, which could reflect different behaviors in the electrolyte solution. The as-prepared substrate surface had a roughness of around 0.5 μm, while the roughness of the coating/substrate interface increased to ~12 μm after spraying, because the WC-Co particles were harder than the substrate and could therefore deform the latter during spraying. This would improve the coating/substrate bonding. The SEM images of the polished surfaces (Fig. 3b and d) showed two distinguishable WC and Co phases. EDS analysis confirmed that the bright phase was WC and the dark phase was cobalt.

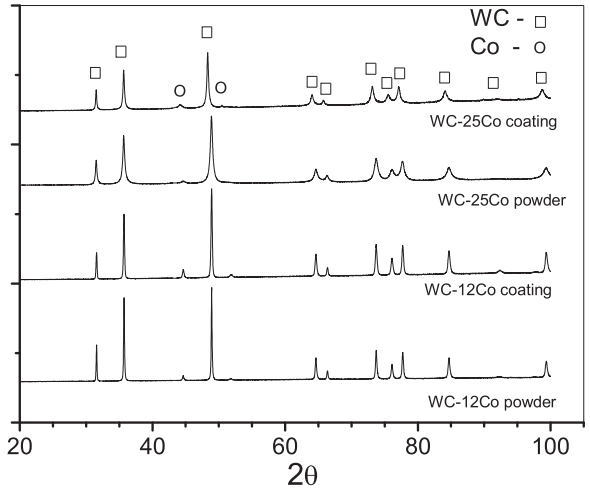

Fig. 2. X-ray diffractograms of the powders and coatings.

The distribution of the WC particles in the Co binder was uniform, which could improve the wear resistance of the WC-Co coatings [11]. The thicknesses were 65 ± 5 μm for WC-12Co and 118 ± 6 μm for WC-25Co. The WC-12Co coating presented a lower thickness because only one layer of material was sprayed; when more than one layer was applied, the deposition became challenging because it was difficult for the WC-12Co powder to deform onto the previously deposited WC-Co. Particle rebound, cavitation of the previously deposited layer, and crack formation were some of the difficulties found when attempts were made to deposit more than one layer. Other studies have also reported difficulty in the deposition of multilayer WC-Co coatings [9,45,57,58]. Kim et al. [45] deposited two layers of WC-12Co coating by spraying, using different spray parameters, but all the coatings showed interconnected porosity and cracks. WC-12Co powder is known to be difficult to deposit by cold spray, due to the low ductility of the WC phase [59], which makes it difficult to reach the critical particle velocity for WC-Co, in addition to the intrinsic high critical velocity for cold spray deposition. Studies have shown that when the ceramic content in the feedstock powder is increased, the overall deposition efficiency decreases, due to in-flight particle interactions and deflection of the particles from the substrate [10,11,59]. In addition, the porosity of the feedstock powder has shown also to play an important role [50]; such porosity helps to accommodate the deformation of the as-sprayed particles.

On the other hand, WC-25Co particles are less hard and more ductile, due to the lower content of the WC phase and the higher proportion of cobalt binder. Therefore, several layers of powder can be sprayed without problems of deflection of the particles.

3.2. Mechanical characterization and hardness testing

The friction wear resistances of the CGS coatings were tested two times with different samples, under a load of 15 N and with initial surface roughness of 0.8 μm (R_a). Wear track profilometric measurements were performed using a confocal laser technique to quantify the material lost, measure the path diameter, and obtain the shape of the wear profile (Fig. 4).

After a sliding distance of 1000 m on the WC-12Co surface coating, the volume lost was $\sim 1.2 \times 10^{-5}\,mm^3\,Nm^{-1}$ and the wear track width was ~810 μm (Table 1). SEM images obtained after the sliding test (Fig. 4a) showed a small loss of material and debris formation at the wear track, indicative of the presence of lubricant W and Co oxides resulting from the high temperatures reached during the sliding. EDS analysis of the debris at specific points along the wear path confirmed the presence of WC and Co oxides that were responsible for the lubricant effect, hence explaining the wear resistance and the loss of almost no material [9].

The WC-25Co coating showed a different wear mechanism. SEM images of the wear tracks showed particles that were pulled out from the coating surface, together with small areas of lubricant oxides (Fig. 4b). The wear mechanism seemed to begin with the extraction of carbides from the matrix, even though the binder phase acts as an excellent support for carbides, and oxides formation due to abrasion [9]. For the WC-25Co coating, the volume lost was $\sim 1.8 \times 10^{-5}\,mm^3\,Nm^{-1}$ and the wear track width was ~830 μm (Table 1).

Due to the WC particle distribution in the ductile binder, together with the absence of brittle or fragile phases, very high sliding resistance was achieved for all the coatings. The wear resistance during testing

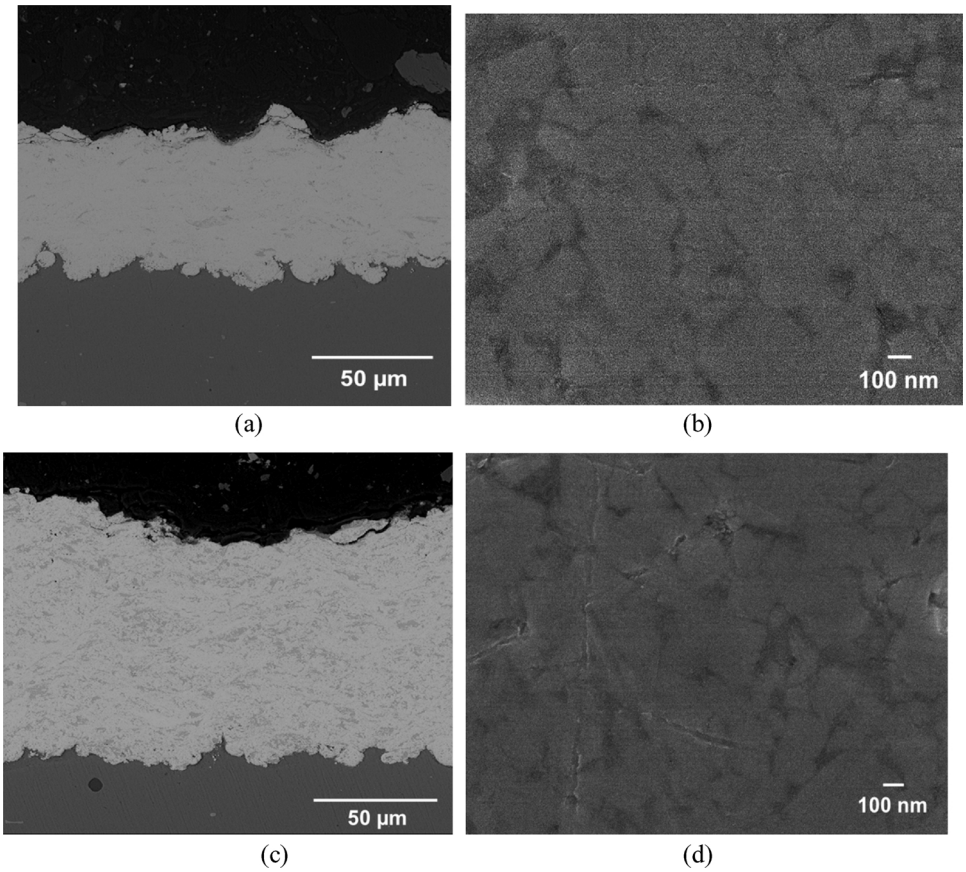

Fig. 3. SEM images of WC-Co coatings on AA 7075-T6. (a) WC-12Co cross-section, (b) WC-12Co polished surface, (c) WC-25Co cross-section, and (d) WC-25Co polished surface.

was higher for the sample with low Co amount (WC-12Co), due to the greater amount of the ceramic phase, in agreement with Couto et al. [11].

The hardness of the AA 7075-T6 substrate was 162 ± 3 HV_{100}, similar to values reported elsewhere [60,61]. The hardness of the WC-25Co coating (754 ± 1 HV) was almost similar to that obtained previously for the same coating prepared by CGS technology, and higher than for a HVOF coating [9,12]. The WC-12Co coating probably had a higher hardness than WC-25Co due to the higher content of the WC phase, as reported elsewhere [62]. However, in the present case, the thickness of the WC-12Co coating was insufficient to allow accurate measurement of the hardness.

3.3. Electrochemical corrosion studies

3.3.1. Open circuit and polarization studies

Firstly, the electrochemical results obtained using short immersion times will be discussed. Fig. 5 shows the E_{OCP} curves for 18 h of immersion in 3.5% NaCl. The E_{OCP} values for the AA 7075-T6 alloy substrate were between −0.7 and −0.8 V *vs.* $Ag|AgCl|KCl_{3mol/L}$, which are typical values for aluminum alloys in chloride solutions containing oxygen [63,64], and tended to stabilize at around −0.78 V *vs.* $Ag|AgCl|KCl_{3mol/L}$. Small potential oscillations were observed, which could have been related to the attack of the oxide layer by chloride ions and repassivation of the surface [65].

The E_{OCP} behaviors for the as-sprayed WC-Co coatings were completely different to that of the AA 7075-T6 substrate. The E_{OCP} values initially decreased, due to dissolution of the oxides at the sample surface, adsorption of chloride, and changes in the local concentrations of oxygen and/or metal ions at the surface [10]. The values then stabilized at around −0.32 V *vs.* $Ag|AgCl|KCl_{3mol/L}$ (WC-12Co) and −0.42 V *vs.* $Ag|AgCl|KCl_{3mol/L}$ (WC-25Co). Under E_{OCP} conditions, the behavior of WC-Co cermets is dominated by dissolution of the less noble component (pure metallic cobalt) and by selective dissolution of metal from the binder phase (Co + WC) [7,14,66,67]. The exposed metallic phase oxidizes from the beginning of the immersion, with the reduction of dissolved O_2 mainly occurring at the WC. Galvanic coupling with the WC component of the material may enhance the rate of dissolution of the Co binder present in the coating, and hydrolysis of the metal cations can lead to acidification of the solution in regions where oxygen access is limited, creating conditions that accelerate corrosion of the cobalt [14,66]. On the other hand, the reduction of oxygen on the carbide phase increases the local pH, and due to the relatively long distance between anodic and cathodic sites, the increase of the pH in the cathodic regions may destabilize the carbide surface [14]. It is notable that the E_{OCP} values reported elsewhere for WC-Co powder [7], measured in the same solution after 26 h of immersion, were in the region of ~ −0.35 V *vs.* $Ag|AgCl|KCl_{sat}$, similar to the values obtained here for the coatings studied, suggesting that the CGS deposition had maintained the original conditions of the powder.

Values of R_P for the substrate and the coated samples were estimated from small amplitude linear polarization measurements after 18 h in 3.5% NaCl solution and were used to determine the corrosion current densities (Table 2). Also shown in Table 2 are the E_{corr} and i_{corr} values obtained from the potentiodynamic polarization curves by the Tafel plot extrapolation method.

Lower i_{corr} (higher R_P) and higher $E_{i\to 0}$ values were obtained for the sample with lower cobalt content. Similar findings, with a slight increase of current density for a sample with higher binder content, were also reported elsewhere [68]. Therefore, the WC-12Co sample seemed to show the best coating performance, in terms of protecting the aluminum alloy substrate against corrosion during short times of immersion in chloride solution, since it presented the most positive E_{corr} and the lowest corrosion current density. Both the higher E_{corr} and the lower

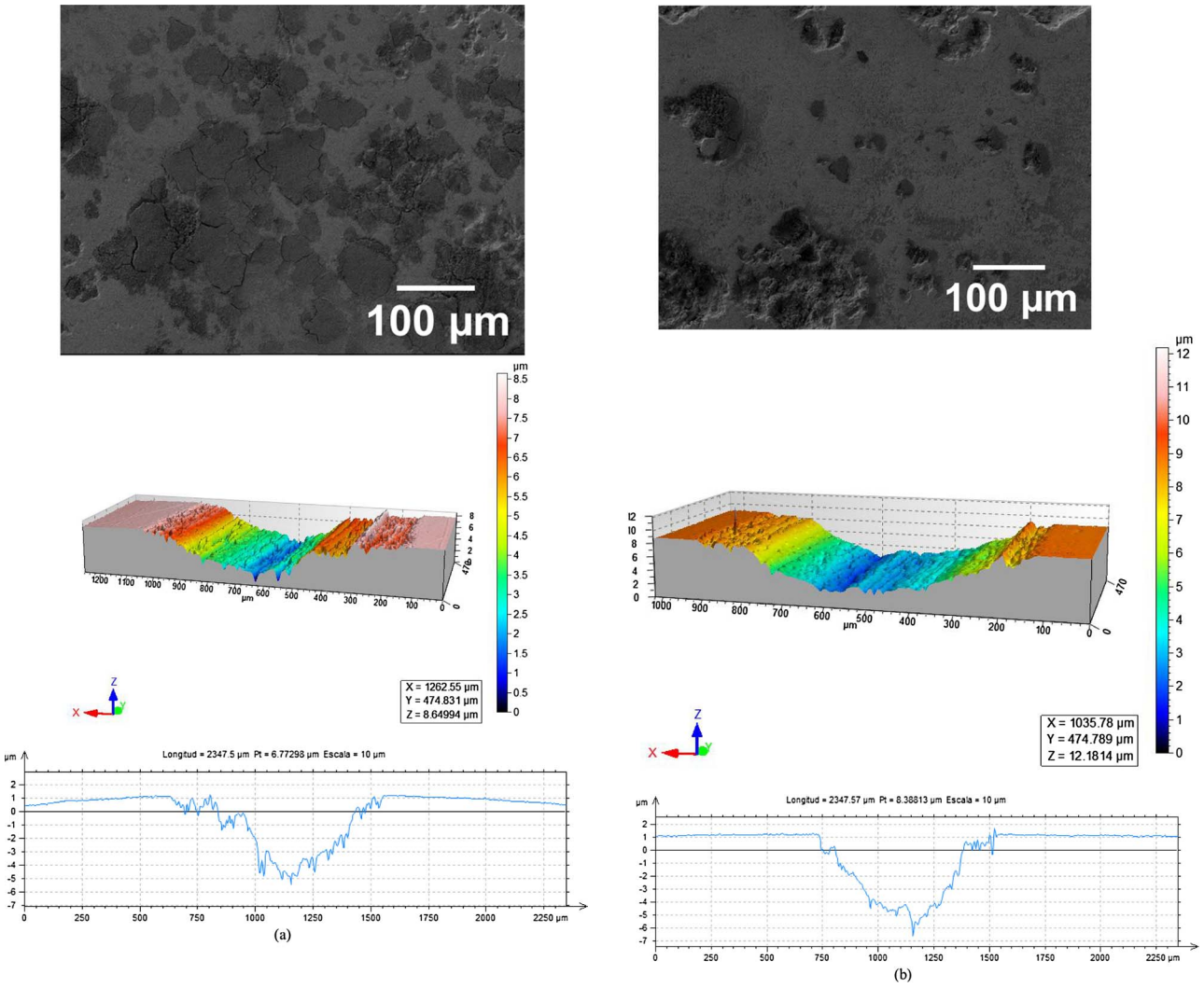

Fig. 4. Morphological features of the wear tracks of the cold sprayed materials: (a) WC-12Co and (b) WC-25Co.

Table 1
Main wear properties of the WC-Co coatings. Two values are given for each system, corresponding to the two measurements made.

Parameter	WC-12Co		WC-25Co	
Friction coefficient	0.50	0.47	0.45	0.46
Volume lost ($mm^3\ Nm^{-1}$)	1.3×10^{-5}	1.1×10^{-5}	1.7×10^{-5}	1.9×10^{-5}
Wear track depth (µm)	810	808	830	837

current density for the WC-12Co sample could be attributed to the smaller relative area of the binder (around 18%, estimated from the image analyses), compared to the WC-25Co sample (relative binder area of around 32%).

Fig. 6 presents the anodic polarization curves for the coatings and the substrate. For the AA 7075-T6, E_{corr} was ~ -0.8 V *vs.* Ag|AgCl|$KCl_{3mol/L}$ and i_{corr} was $\sim 2.5\ \mu A\ cm^{-2}$. The polarization curve for the substrate (Fig. 6a) showed a rapid increase of the current when the potential reached -0.70 V *vs.* Ag|AgCl|$KCl_{3mol/L}$, due to pitting corrosion. The first breakdown potential [51,67,69] was poorly defined, despite the fact that the substrate surface was mechanically treated, but there was a well-defined pitting potential at -0.72 V *vs.* Ag|AgCl|$KCl_{3mol/L}$. Anodic and cathodic aluminum corrosion processes in chloride medium at pH near 7 involve the dissolution of aluminum and the reduction of dissolved oxygen, respectively, according to the following reactions [65]:

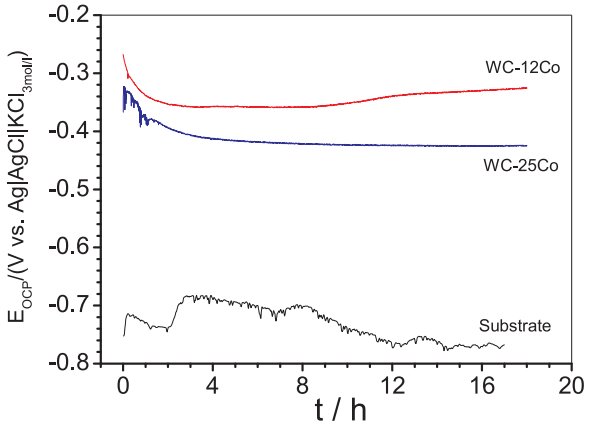

Fig. 5. Plots of open circuit potential according to time for all samples studied, measured during relatively short immersion in aerated and unstirred 3.5 wt% NaCl solution at 25 °C.

$$Al \rightarrow Al^{3+} + 3e^- \quad (1)$$

$$O_2 + 2H_2O + 4e^- \rightarrow 4OH^- \quad (2)$$

Hence, Al^{3+} ions can react with OH^- ions to form aluminum hydroxide near the aluminum surface, according to the global equation:

Table 2
Corrosion parameters estimated from small amplitude linear polarization and potentiodynamic polarization curves after 18 h of immersion in 3.5 wt% NaCl solution.

Parameter	AA 7075-T6	WC-12Co	WC-25Co
$^{*}E_{i\rightarrow 0}$ (mV *vs.* Ag|AgCl|$KCl_{3mol/L}$	−814 ± 2	−326 ± 4	−425 ± 2
E_{corr} (mV *vs.* Ag|AgCl|$KCl_{3mol/L}$	−831 ± 2	−336 ± 2	−425 ± 1
[a]i_{corr} (μA cm^{-2})	10.7	28	30
[b]i_{corr} (μA cm^{-2})	2.9	10	23
b_a (mV dec^{-1})	82.5	148	111

[a] i_{corr} values obtained using the Stern-Geary equation, $i_{corr} = b_a/2.3 \times R_p$, where b_a is the anodic Tafel plot slope and R_p is the polarization resistance.
[b] i_{corr} values obtained using the Tafel plot extrapolation method.

$$Al^{3+} + 3OH^- \rightarrow Al(OH)_3 \quad (3)$$

The aluminum hydroxide can precipitate on the surface, due to its low solubility product, and gradually change to aluminum oxide, resulting in the formation of a passive film:

$$2Al(OH)_3 \rightarrow Al_2O_3 + 3H_2O \quad (4)$$

This normally occurs on aluminum or aluminum alloy surfaces. For aluminum alloys containing intermetallic compounds, as in the case of the AA 7075-T6 alloy, this kind of oxide film does not cover the entire electrode surface and/or offer sufficient protection against the attack of chloride anions that leads to pitting formation. This explained the rapid increase of current when high overpotentials were reached. It was also clear that the anodic Tafel plot slope could not be obtained by extrapolation of the Tafel lines, and only E_{corr} could be estimated (Table 2).

The anodic polarization measurements for the coatings (Fig. 6a) revealed a gradual current increase as a more positive overpotential was applied. The corrosion potential of the WC-12Co coating shifted to more positive values, with $E_{corr} = -0.33$ V *vs.* Ag|AgCl|$KCl_{3mol/L}$ and $i_{corr} = 1.2\,\mu A\,cm^{-2}$, while the corresponding values for the WC-25Co coating were -0.42 V *vs.* Ag|AgCl|$KCl_{3mol/L}$ and $2.9\,\mu A\,cm^{-2}$. These values were slightly lower than the E_{corr} values obtained for WC-Co with similar composition in aqueous solutions of $0.5\,mol\,L^{-1}$ H_2SO_4 [68] and $0.05\,mol\,L^{-1}$ NaCl [66]. The anodic and cathodic processes of WC-Co corrosion in chloride solution correspond to the following reactions: dissolution of Co (Eq. (5)) and reduction of dissolved oxygen on the WC phase (Eq. (2)) [14,66].

$$Co \rightarrow Co^{2+}_{(aq)} + 2e^- \quad (5)$$

In the absence of oxygen and aggressive anions, various metallic oxides may be formed on the WC-Co surface during the anodic polarization, with Co being oxidized to CoO, forming an inner layer, and to $Co_{3-x}O_4$, as an outer layer [14,34,70]:

$$Co + 3H_2O \rightarrow CoO + 2H_3O^+ + 2e^- \quad (6)$$

$$Co + 4H_2O \rightarrow Co(OH)_2 + 2H_3O^+ + 2e^- \quad (7)$$

$$3CoO + 3H_2O \rightarrow Co_3O_4 + 2H_3O^+ + 2e^- \quad (8)$$

$$3Co(OH)_2 \rightarrow Co_3O_4 + 2H_3O^+ + 2e^- \quad (9)$$

$$Co_3O_4 + 6H_2O \rightarrow 3Co(OH)_3 + H_3O^+ + e^- \quad (10)$$

However, in the presence of chloride ions, the formation of such oxides is not able to make the surface passive, due to the high chloride activity. Under open-circuit conditions or with small positive applied potentials, the binder phase undergoes selective dissolution, but when higher potential is applied, dissolution of the WC phase also takes place [14]. Cathodic curves (Fig. 6b) obtained in the presence of oxygen showed two current plateaus, which were attributed to the reduction of oxygen, in the range from −0.5 to −0.9 V *vs.* Ag|AgCl|$KCl_{3mol/L}$, and to the reduction of water at more negative potentials. Fig. 6c compares cathodic curves obtained in the absence and presence of oxygen. In the presence of oxygen, a fast electrochemical reaction (diffusion controlled) was observed, while in its absence, the main process was the reduction of water and the evolution of hydrogen (Eq. (11)).

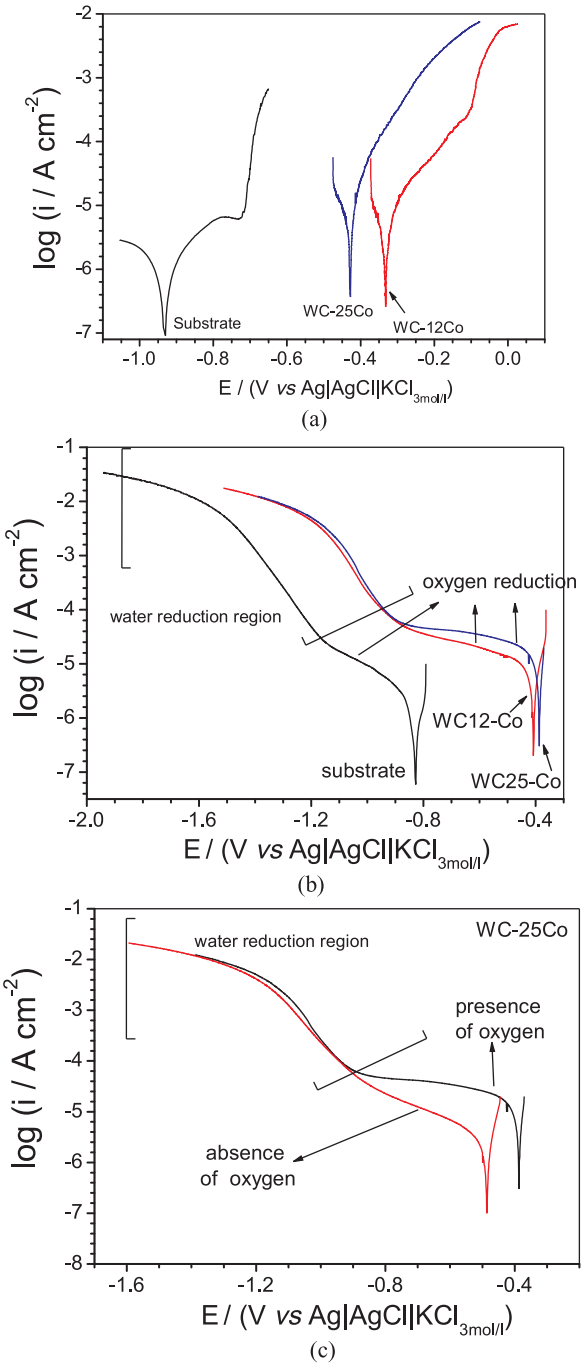

Fig. 6. (a) Anodic and (b) cathodic potentiodynamic polarization curves for the AA 7075-T6 alloy and the coated samples, recorded at $0.166\,mV\,s^{-1}$ in unpurged and quiescent 3.5 wt% NaCl solution after ~18 h of immersion. (c) Cathodic curves for the WC-25Co coating obtained in the same solution in the presence and absence of oxygen.

$$2H_2O_{(l)} + 2e^- \rightarrow H_{2(g)} + 2OH^-_{(aq)} \quad (11)$$

The cathodic reduction of both water and oxygen shifts the local solution pH towards higher values. An investigation of the pH dependence of the WC phase demonstrated its instability in the alkaline pH 9–14 range, which might make it susceptible to chemical dissolution, according to Eq. (12) [14,71]:

$$WC + 6H_2O \rightarrow WO_4^{2-} + CO_2 + 12H^+ + 10e^- \quad (12)$$

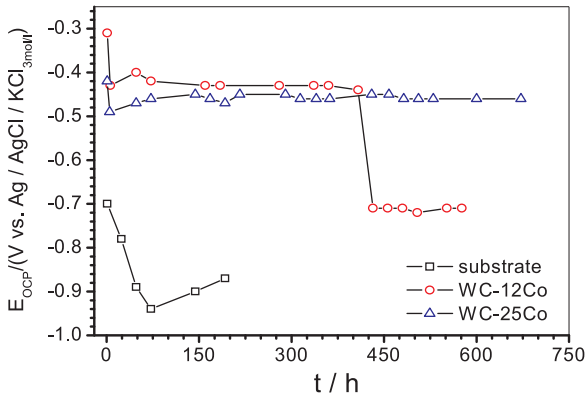

Fig. 7. Open circuit potentials for the substrate and the coatings, as a function of time, measured in aerated and unstirred 3.5 wt% NaCl solution during long immersion times, at 25 °C.

At potentials more negative than -1.0 V *vs.* Ag|AgCl|$KCl_{3mol/L}$, the evolution of hydrogen (water reduction reaction) and the dissolution of carbide occur, leading to an increase of the current.

Cross-sectional SEM images obtained after anodic potentiodynamic polarization (Fig. 3S, *SD*) showed that brittle zones were formed in the coatings, encompassing the entire cross-section, in the case of the WC-12Co sample (Fig. 3Sa, *SD*), and the region between 10 and 30 µm from the top, for WC-25Co (Fig. 3Sb, *SD*). Cracks in these zones readily developed during preparation of the cross-sections. The greater extent of the defects for the sample with less cobalt could be attributed to the lower binder content and the higher porosity. The applied potential favored the increase of stress in this region, due to acceleration of the growth of oxides and electrolyte penetration, but the bottom of the coating was not affected by the polarization.

The substrate (AA 7075-T6) and the coatings were also examined by E_{OCP} measurements for long immersion times of 196 h (AA 7075-T6 substrate), ~600 h (WC-12Co), and ~700 h (WC-25Co). For AA 7075-T6 (Fig. 7), the E_{OCP} value at 1 h of immersion was around −0.70 V *vs.* Ag|AgCl|$KCl_{3mol/L}$, followed by a decrease to ~−0.95 V *vs.* Ag|AgCl|$KCl_{3mol/L}$ and then an increase to −0.85 V *vs.* Ag|AgCl|$KCl_{3mol/L}$. This indicated that native oxides and oxides initially formed on the substrate surface when exposed to the aqueous solution were responsible for the relatively high open circuit potential [66,72]. However, this oxide film was not sufficiently protective, and the potential decreased to around −0.8 V *vs.* Ag|AgCl|$KCl_{3mol/L}$ at 24 h, with attainment of a minimum value of −0.95 V *vs.* Ag|AgCl|$KCl_{3mol/L}$ at ~70 h (due to localized corrosion that exposed the aluminum surface to the electrolyte), followed by an increase for longer immersion times, reaching −0.85 V *vs.* Ag|AgCl|$KCl_{3mol/L}$ after 196 h of immersion.

For the coatings, the E_{OCP} values decreased in the first hours of immersion (Fig. 7), possibly indicating the dissolution of native oxides present at the surface, due to the adsorption and attack of chloride ions with negative charge. The dissolution of native oxide could then have exposed the cobalt matrix, which is a more active phase, leading to the decreases of the open circuit potential. After 48 h of immersion, the potentials reached around −0.44 V *vs.* Ag|AgCl|$KCl_{3mol/L}$ (WC-12Co) and −0.42 V *vs.* Ag|AgCl|$KCl_{3mol/L}$ (WC-25Co), probably due to the formation/dissolution of corrosion products, especially dissolution of cobalt. The E_{OCP} values suggested that the electrolyte did not reach the substrate in the first hours of immersion, since the potential for the substrate was ~−0.85 V *vs.* Ag|AgCl|$KCl_{3mol/L}$.

In order to understand the corrosion process that occurred at open circuit potential during an extended immersion time, microscopy analyses of the surface of the WC-12Co coating were performed before the immersion in 3.5% NaCl and again after 96 h (Fig. 8). Image analysis revealed an almost oxide-free coating, which could explain the initial decrease in the E_{OCP} value. The small variation of potential could be

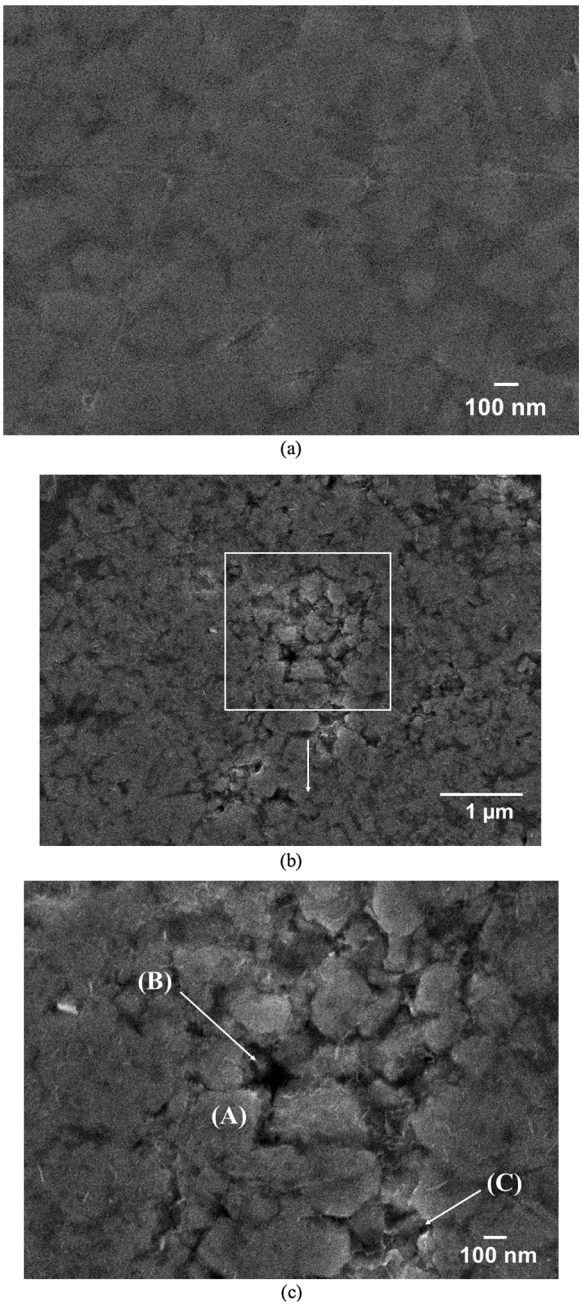

Fig. 8. SEM images of (a) the polished WC-12Co coating surface, (b) the corroded area after 96 h of immersion in 3.5% NaCl, and (c) the region indicated in (b), at higher magnification, showing (A) intact WC particles, (B) deep attack to specific sites of the cobalt phase, and (C) loss of the WC particles.

explained by the formation/dissolution of corrosion products, particularly on the surface near WC particles, where chloride ions adsorbed onto the cobalt binder. Small coating defects, mainly around the WC particles, together with galvanic effects, assisted the accelerated dissolution of the Co phase at specific sites (Fig. 8b), generating deep attack in these areas (Fig. 8c (B)), as observed previously [66]. A comparison of the cross-sectional SEM images at 20 µm from the top, for both coatings and at the end of the E_{OCP} measurements (Fig. 4S, *SD*), revealed large holes in the case of WC-12Co, indicative of greater damage of this coating and supporting the hypothesis provided below to explain the EIS results. Corrosion around the WC phase could be explained by the known formation of local cells between the WC phase (nobler) and the Co matrix (more active) [68]. No signs of corrosion were observed on WC after 96 h of immersion, although corrosion

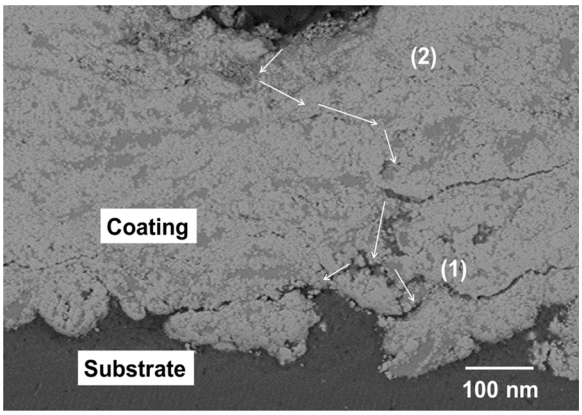

(a)

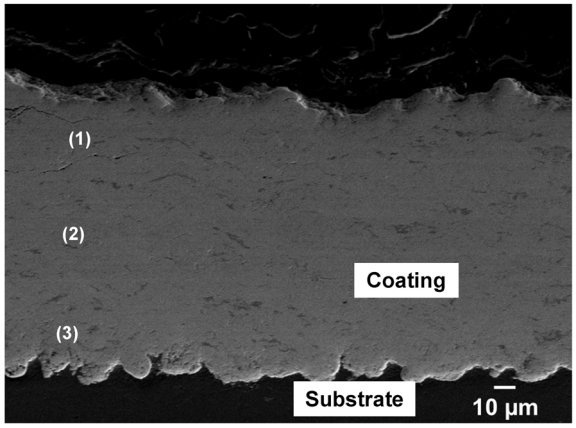

(b)

Fig. 9. Cross-sectional SEM images of (a) the WC-12Co coating after 600 h, and (b) the WC-25Co coating after 700 h in 3.5 wt% NaCl. The numbers indicate the sites where EDS analyses were performed.

might occur with longer exposure times, since the local pH becomes alkaline due to the oxygen reduction [66,67]. The preferential dissolution of Co could cause the detachment of WC particles, even if they are insoluble (Fig. 8c (C)), resulting in a rough appearance of the surface (Fig. 8a). The dissolution of the Co phase and the loss of WC particles could lead to interconnected porosity and paths allowing diffusion of the electrolyte through the coating until reaching the substrate. This process, as well as the lower thickness of WC-12Co, could explain the fast decrease of E_{OCP} for this sample after 400 h of immersion (Fig. 7), reaching −0.71 V *vs.* Ag|AgCl|$KCl_{3mol/L}$, a value very close to that obtained for the substrate, suggesting that the electrolyte may have reached the substrate.

SEM cross-sectional images of the WC-12Co coating showed severe damage at the top of the coating, with pathways allowing the electrolyte to reach the substrate at specific points, but not over the entire coating/substrate interface (Fig. 9a). EDS analysis at spots 1 and 2 detected the following elements: (spot 1) oxygen (3 wt%), cobalt (24 wt %), tungsten (70 wt%), and a small amount of aluminum (3 wt%); (spot 2) oxygen (5 wt%), Co (20 wt%), and W (75 wt%). The oxygen content was higher near the surface, while the percentage of cobalt decreased at the top of the coating, due to greater metal dissolution. This indicated that a larger area had been attacked at the top than at other regions of the coating. An important point to note is that the top of the coating presented higher roughness than the substrate. The presence of aluminum at some spots indicated that the electrolyte had only reached the substrate in some areas, rather than over the entire coating/substrate interface.

For the WC-25Co coating, the E_{OCP} values remained constant even after 700 h of immersion. After the test, the SEM cross-sectional images for WC-25Co (Fig. 9b) showed no corrosion of the substrate, probably due to the thicker coating, compared to WC-12Co. Only small amount of oxides were present near the top surface. Cracks within the coatings, at around 40 µm from the top, probably developed during preparation of the cross-sections. EDS analysis (Fig. 5S, *SD*) of the corroded cross-section (Fig. 9b) revealed the presence of only tungsten, carbon, cobalt, and oxygen. Aluminum was not detected, indicating that the electrolyte had not reached the substrate, even after ~700 h of immersion.

3.3.2. Electrochemical impedance studies

Electrochemical impedance spectroscopy measurements were performed for all the samples, at 24 h intervals, during different immersion times depending on the response of the coating. The WC-12Co coating was studied up to 600 h, since the open circuit potential values suggested degradation of the coating at around 400 h. The substrate was studied up to 192 h.

Fig. 6S (*SD*) shows the EIS diagrams for the AA 7075-T6 alloy at immersion times from 1 h up to 192 h. At 1 h, the complex plane showed only one time constant, which was probably due to the native aluminum oxide response, while at later immersion times, two time constants were apparent (Fig. 6S, *SD*), which could be explained by the charge transfer process associated with aluminum oxidation/oxygen reduction, together with the response of the corrosion products. The native oxide had low resistance to the chloride attack and could be degraded or dissolved within a few hours of immersion in chloride solution, so it had a minor influence on the charge transfer resistance that dominated the response. Over the course of time, pits were formed, the corrosion products precipitated on the electrode surface, and two time constants were still apparent. It is also interesting to note that the system exhibited instability for some immersion times (Fig. 6Sa, *SD*), while it remained stable for other immersion times (Fig. 6Sa, *SD*). The instability was reflected by dispersion at low frequency (LF), with evidence of inductive behavior caused by the pitting development. The Bode plots (ϕ *vs.* log (f)) (Fig. 6Sb) showed a large maximum at medium frequencies (MF), centered at ~25 Hz, with a phase angle of around -80°, which is typical of a capacitive system. Small differences in the Bode modulus of impedance *vs.* frequency with the immersion time were observed in the LF region. Due to the instabilities shown in the impedance diagrams for certain immersion times, no fitting with electrical equivalent circuits was performed for any of them.

Figs. 10 and 11 show the impedance moduli (|Z|) and Bode phase angles, and complex plane (Fig. 7S) plots illustrating the impedance responses of the two coated samples immersed in chloride solution for 24 h and ~600 h. The solid lines correspond to the fitting of the impedance data.

For 24 h of immersion, the complex plane plot for the WC-25Co coating showed one asymmetric and incomplete semicircle, while for the WC-12Co coating, a second time constant was apparent at low

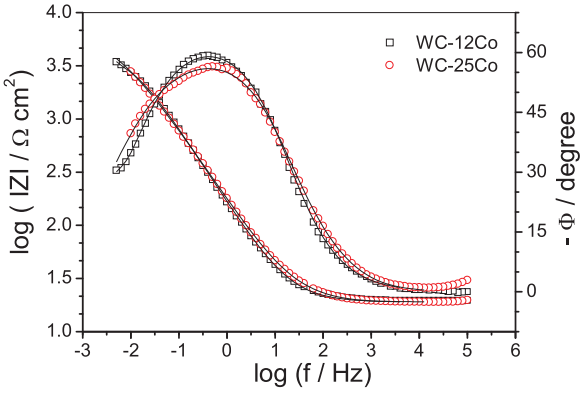

Fig. 10. Experimental (symbols) and fitted (solid lines) Bode phase plots obtained for the coated samples immersed for 24 h in 3.5 wt% NaCl solution at 25 °C.

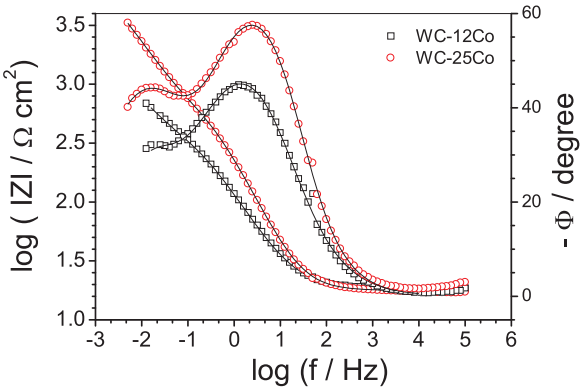

Fig. 11. Experimental (symbols) and fitted (solid lines) Bode phase plots obtained for the coated samples immersed for ~600 h in 3.5 wt% NaCl solution at 25 °C.

frequency (Fig. 7Sa, *SD*). The Bode plots (ϕ *vs*. log (f)) showed one large time constant in the MF to LF range (Fig. 10). The shape of this plot suggested the presence of more than one time constant, which was confirmed when the experimental data were treated using electrical equivalent circuits. For both coatings, the Bode plots (Fig. 10) showed a phase angle maximum at −57° (~0.3 Hz). For short immersion times, there appeared to be no substantial difference between the impedance values of the two samples, as could be observed from the modulus of impedance.

EIS diagrams showing the impedance behaviors of the coatings in chloride solution after ~600 h of immersion are provided in Figs. 11 and 7Sb (*SD*). The complex plane plots (Fig. 7Sb (*SD*)) exhibited two asymmetric semicircles, with greater amplitude for the WC-25Co coating. The Bode plot (Fig. 11) showed two time constants, one in the MF region and another (less well defined) in the LF region, with phase angles of −44° for WC-12Co and −57° for WC-25Co (in the latter case, the value was similar to the value obtained during the initial immersion period). The reduction of the capacitive arc and phase angle values for WC-12Co suggested that the ability of the coating to protect the substrate decreased, which could be attributed to the electrolyte accessing the substrate through the defects in the coating. On the other hand, no decrease in the impedance was observed for the WC-25Co coating, which could be attributed to the higher barrier effect of the coating, due to its greater thickness. As mentioned earlier, WC-25Co particles are more ductile, so during the spraying process there is greater plastic deformation of the particles following impact with the substrate or with the previously deposited layers. This results in increased deposition efficiency and the formation of a thicker and more compact coating, leading to better corrosion performance [9].

The EIS results were also quantitatively analyzed using electrical equivalent circuit theory, with EECs being chosen considering the structures of the coated samples, the best fitting of the experimental data, and the lowest residual error of each parameter from the equivalent circuit. The EIS diagrams for the AA 7075-T6 alloy were not fitted, since some of them showed dispersion at low frequencies, as mentioned above.

For the coatings, the following observations were considered in selection and justification of the electrical equivalent circuits: (a) the oxide contents detected on the electrode surfaces were very low, including at the end of the experiment, as demonstrated by the EDS analysis (Fig. 5S), even considering that the EDS measurements were limited in terms of their suitability for quantitative analyses of light elements such as oxygen. This indicated that under the conditions employed here, the main processes were dissolution of cobalt (from the binder) and reduction of oxygen (on WC particles); (b) for all immersion times, no signs of passivation were observed for either coating, indicating that cobalt was continuously dissolved. Some metallic regions dissolved faster, leading to features such as pits (Fig. 8b) that could continuously undermine the coating, and the attack could also propagate laterally [66]; (c) oxygen was mainly reduced at the electrode surface, because access to the inner regions of the sample was limited [66]. As a consequence, increase of the local pH at long immersion times could destabilize the cathodic surface (the WC phase); (d) the electrolyte apparently did not reach the substrate until ~400 h for the WC-12Co coating and ~700 h for the WC-25Co coating, as indicated by the high open circuit potential values for the two coatings at those immersion times (Fig. 7); (e) after 500 h of immersion, EDS analysis of the WC-12Co coating detected Al and some alloying elements at specific points near the substrate, indicating that the solution had reached the substrate (Fig. 9a), as also suggested by the sharp decrease of E_{OCP} after 400 h (Fig. 7). The WC-25Co coating/substrate interface remained intact (Fig. 9b), with no Al or alloying elements detected within the coating near the substrate, indicating that the solution did not reach the substrate during the immersion time. For the same reason, E_{OCP} remained constant throughout the immersion time (Fig. 7).

The dissolution of metallic cobalt can be accelerated because hydrolysis of the Co^{2+} ions acidifies the medium locally [73], increasing the deep dissolution of cobalt in some regions of the binder, with greater sub-surface corrosion that may extend laterally to the surface. The reduction of oxygen at the cathodic sites (the WC phase) can increase the local pH, since these sites are separated from the anodic sites, which could facilitate WC dissolution [14,66].

The observations described above concerning the characteristics of the system studied, together with literature reports [14,66–68], enabled interpretation of the EIS data in a similar way as employed recently for cemented carbides [66], adopting the EECs shown in Fig. 12a and b. In these circuits, R_s is the solution resistance, and a constant phase element (CPE) substitutes the capacitor to account for the effect of the heterogeneities of charge distribution at the electrode surface [74]. The CPE represents a non-ideal capacitor and can be a resistance (exponent $n = 0$), an ideal capacitor ($n = 1$), a Warburg resistance ($n = 0.5$), or an ideal inductor ($n = -1$) [74].

At short immersion times, the responses of the systems showed one time constant. Considering that oxides were practically absent, the only processes that occurred were likely to have been the oxidation of cobalt from the binder and the reduction of oxygen on the WC phase, which were represented by a capacitance in parallel with an R(RC) network. $R_{ct}//CPE_{dl}$ denotes the cathodic and anodic charge transfer resistance (cobalt oxidation and oxygen reduction) and the electrical double layer

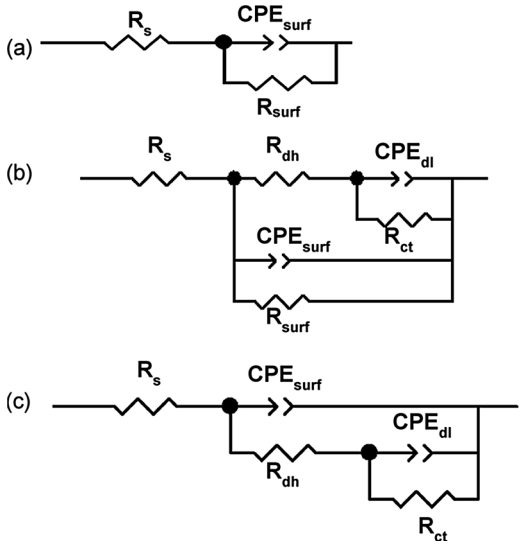

Fig. 12. Electrical equivalent circuits (EECs) used to analyze the impedance data of the coatings: (a) for the first hours of immersion; (b) interpretation of EIS data after some immersion time; (c) EEC used to fit the EIS data after a few hours of immersion.

of the cathode and anode. These were reduced to one *R//CPE* sub-circuit (Fig. 12a). However, this simple circuit could encompass all the contributions arising from the global surface, such as resistances and capacitances associated with the charge transfer process, as well as contributions from an existing incipient film, or one eventually formed by the accumulation of corrosion products on the surface. This simple sub-circuit could be represented as $R_{surf}//CPE_{surf}$, with domination of the lowest resistance and the highest capacitance of processes developing at the surface. After some time (for example, 24 h), a new time constant was required in order to fit the experimental results, as observed previously for WC-Co composite and cemented carbides by Oliveira et al. [66]. This second time constant could be attributed to the rapid dissolution of cobalt from the binder at specific sites, such as binder defects or points surrounding the WC phase, where the galvanic effect could accelerate cobalt dissolution, producing holes (Fig. 8b). As the holes became deeper, the attack on the binder could propagate laterally through defects between splats, increasing the damage to the coating. Hence, the solution within the holes added a new resistance (R_{dh}) to the system, separating the process occurring within the holes from that at the surface. Therefore, the $R_{ct}//CPE_{dl}$ sub-circuit could account for the dissolution of cobalt within the holes and within the coating, and the system could be described by the circuit shown in Fig. 12b. As the experiment progressed, R_{dh} increased relative to R_{surf}, and when $R_{surf} < R_{dh}$, the EEC shown in Fig. 12b changed to that shown in Fig. 12c. In the present work, it appeared that $R_{surf} < R_{dh}$ was reached after around 24 h of immersion, so the EIS data obtained after 24 h of immersion were fitted using the EEC shown in Fig. 12c. The parameter values of the different elements of the circuits employed for the coatings are given in Tables 1S and 2S (*SD*). In this circuit, R_s represents the solution resistance. The suitability of the proposed EECs was indicated by Chi-squared (χ^2) deviation values of around 10^{-4}, relatively low standard errors (< 10%) for each parameter (Tables 1S and 2S, *SD*), and good agreement between the fitted and experimental EIS plots (Figs. 10 and 11, and 7S). An EEC similar to that shown in Fig. 12c was used previously to treat impedance data obtained for a CGS zinc coating applied to a mild steel substrate [75].

Given that only the cobalt was dissolved, the polarizations and charge transfer resistances could be recalculated considering only the dissolution areas: ~18% and ~32% for WC-12Co and WC-25Co, respectively. This recalculation could provide R_p and R_{ct} values closer to those expected for the cobalt dissolution areas during the first hours of immersion and has been used previously for the same purpose [14,64,67]. However, it should be used with caution for longer immersion times, because the area of cobalt dissolution becomes difficult to estimate, due to the development of holes and attack on other defects of the coating. On the other hand, since R_{surf} was removed from the EEC (Fig. 12c) and the correction of the area was no longer considered, the contribution of the surface to the total cobalt dissolution was of minor significance. Fig. 13 provides the corrected R_{ct} and R_{dl} values for the two coatings, with WC-12Co showing large decreases in both resistances at around 400 h of immersion, while the resistances tended to continuously increase in the case of WC-25Co.

This behavior could be explained considering that for WC-12Co, the electrolyte reached the substrate at around this immersion time (~400 h), while for WC-25Co the coating/substrate interface remained intact, as also indicated by the cross-sectional SEM images (Fig. 9). The lower performance of WC-12Co could also be attributed to its higher porosity and greater difficulty of plastic deformation of the particles due to the lower binder content, which could lead to a greater quantity of defects. For WC-12Co, R_{dh} increased rapidly up to around 400 h of immersion and then abruptly decreased to a very low value. The increase could be explained by increase of the depth of holes, until a maximum value was reached, followed by a decrease when the electrolyte reached the coating/substrate interface. At this point, the dissolution mechanism shifted to include a contribution from Al dissolution, with very low resistance of the corrosion products at the bottom of the holes because the hydrolysis of aluminum ions decreased the local pH and the dissolution of Al continued (see Fig. 9). The reduction of oxygen was essentially limited to the surface of the sample.

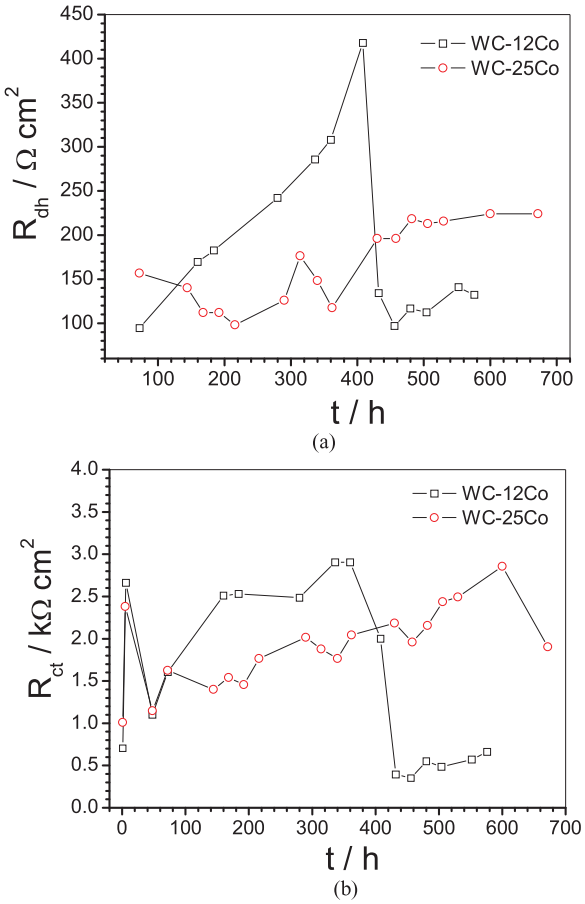

Fig. 13. (a)R_{dh} and (b) R_{ct} for the WC-Co coatings in 3.5% NaCl solution at 25 °C.

E_{OCP} and EIS results reported previously for WC-Co coatings prepared on an Al substrate using the HVOF technique showed low corrosion resistance, compared to CGS coatings [7]. The high temperature used during the HVOF spray process leads to undesirable effects such as decarburization, formation of W_2C, W, and/or fragile phases, and the presence of pores and cracks. The formation of new phases makes the coating more heterogeneous, while the formation of local cells during the electrochemical tests increases the corrosion rate [13,7,12,37–39]. The cracks and pores provide pathways for electrolyte diffusion, allowing the electrolyte to reach the coating/substrate interface at immersion times up to 50 h [7].

In the salt spray tests, the images of the coating surfaces showed no signs of substrate corrosion after 500 h (Fig. 8S, *SD*). However, after 1000 h, small corrosion spots appeared on the WC-12Co coating, while the WC-25Co coating was apparently not corroded at the surface. Therefore, the test was continued up to 3000 h (Fig. 8S, *SD*), when a more corroded surface was observed for WC-12Co (Fig. 8Sa, *SD*), compared to WC-25Co (Fig. 8Sb, *SD*). In order to confirm these observations, the surfaces of the coatings were analyzed by EDS (Fig. 9S, *SD*). Aluminum was detected on the WC-12Co surface (Fig. 9Sa, *SD*), but not on the WC-25Co surface (Fig. 9Sb, *SD*), corroborating the better performance of this coating, as indicated by all the results described above. It is also interesting to note that a very simple experiment involving E_{OCP} measurement (Fig. 7) was able to reveal the damage to the WC-12Co coating caused by the salt spray test. Comparison of the results of salt fog spray tests obtained for a WC-12Co coating prepared by HVOF [37] using conventional powder (resistant for 130 h) and nanostructured powder (resistant for 600 h), and the same coating

prepared by CGS technology (first signs of corrosion after 1000 h), clearly evidenced the superiority of the CGS technique. The result for the WC-25Co coating prepared by CGS was much more impressive, since it remained practically unaltered after 3000 h of the salt fog test, indicating the very high performance of this coating.

4. Conclusions

The results showed that the CGS technique has great potential to produce carbide coatings. The sprayed coatings showed well distributed ceramic phases, no cracks, low porosity, and apparently no interconnected pores.

The WC-12Co coating was corrosion resistant during at least 400 h of immersion in 3.5% NaCl solution. At longer immersion times in 3.5% NaCl, dissolution of the cobalt phase and the loss of WC particles led to the formation of interconnected porosity, allowing access of the electrolyte and corrosion of the substrate. The low thickness, higher porosity, and probably a greater quantity of defects were responsible for weaker performance of this coating.

The compactness, low porosity, and thickness of the WC-25Co coating enabled it to protect AA 7075T6 against corrosion for at least ~700 h of immersion in 3.5% NaCl solution, as corroborated by the fact that both resistance and capacitance remained almost constant during the period of the experiment. The WC-25Co coating withstood 3000 h exposure in the salt fog spray test with neutral 5 wt% NaCl at 35 °C, indicating a very high performance against corrosion under these conditions.

The compressive effect of applying the particles using the CGS technique, the appropriate amount of binder, and optimization of spray parameters, resulting in a less porous coating, were the main factors responsible for the high mechanical and anti-corrosion performance of the WC-25Co coating.

Acknowledgements

The authors would like to thank CNPq (Conselho Nacional de Pesquisa, grants 153177/2014-4 and 201325/2014-4) for financial support and scholarships.

Appendix A. Supplementary data

Supplementary material related to this article can be found, in the online version, at doi:https://doi.org/10.1016/j.corsci.2018.03.010.

References

[1] D. Dzhurinskiy, E. Maeva, E. Leshchinsky, R.G. Maev, Corrosion protection of light alloys using low pressure cold spray, J. Therm. Spray Technol. 21 (2012) 304–313, http://dx.doi.org/10.1007/s11666-011-9729-7.
[2] R.G. Buchheit, R.P. Grant, P.F. Hlava, B. Mckenzie, G.L. Zender, Local dissolution phenomena associated with S phase (Al[sub2]CuMg) particles in aluminum alloy 2024-T3, J. Electrochem. Soc. 144 (1997) 2621–2627, http://dx.doi.org/10.1149/1.1837874.
[3] A.S. El-Amoush, Intergranular corrosion behavior of the 7075-T6 aluminum alloy under different annealing conditions, Mater. Chem. Phys. 126 (2011) 607–613, http://dx.doi.org/10.1016/j.matchemphys.2011.01.010.
[4] S. Maitra, G.C. English, Mechanism of localized corrosion of 7075 alloy plate, Metall. Trans. A 12 (1981) 535–541, http://dx.doi.org/10.1007/BF02648553.
[5] O. Meydanoglu, B. Jodoin, E.S. Kayali, Surface & coatings technology microstructure, mechanical properties and corrosion performance of 7075 Al matrix ceramic particle reinforced composite coatings produced by the cold gas dynamic spraying process, Surf. Coat. Technol. 235 (2013) 108–116, http://dx.doi.org/10.1016/j.surfcoat.2013.07.020.
[6] N. Birbilis, R.G. Buchheit, Electrochemical characteristics of intermetallic phases in aluminum alloys, J. Electrochem. Soc. 152 (2005) B140–B151, http://dx.doi.org/10.1149/1.1869984.
[7] M. Magnani, P.H. Suegama, N. Espallargas, C.S. Fugivara, J.M. Guilemany, A.V. Benedetti, Influence of HVOF parameters on the corrosion and wear resistance of WC-Co coatings sprayed on AA7050 T7, Surf. Coat. Technol. 202 (2008) 4746–4757, http://dx.doi.org/10.1016/j.surfcoat.2008.04.055.
[8] J.A. Picas, A. Forn, R. Rilla, E. Martin, HVOF thermal sprayed coatings on aluminium alloys and aluminium matrix composites, Surf. Coat. Technol. 200 (2005) 1178–1181, http://dx.doi.org/10.1016/j.surfcoat.2005.02.124.
[9] S. Dosta, M. Couto, J.M. Guilemany, Cold spray deposition of a WC-25Co cermet onto Al7075-T6 and carbon steel substrates, Acta Mater. 61 (2013) 643–652, http://dx.doi.org/10.1016/j.actamat.2012.10.011.
[10] M. Couto, S. Dosta, J.M. Guilemany, Comparison of the mechanical and electrochemical properties of WC-17 and 12Co coatings onto Al7075-T6 obtained by high velocity oxy-fuel and cold gas spraying, Surf. Coat. Technol. 268 (2014) 180–189, http://dx.doi.org/10.1016/j.surfcoat.2014.04.034.
[11] M. Couto, S. Dosta, M. Torrell, J. Fernández, J.M. Guilemany, Cold spray deposition of WC-17 and 12Co cermets onto aluminum, Surf. Coat. Technol. 235 (2013) 54–61, http://dx.doi.org/10.1016/j.surfcoat.2013.07.011.
[12] M. Couto, S. Dosta, J. Fernandez, J.M. Guilemany, Comparison of the mechanical and electrochemical properties of WC-25Co coatings obtained by high velocity oxy-fuel and cold gas spraying, J. Therm. Spray Technol. 23 (8) (2014) 1251–1258, http://dx.doi.org/10.1007/s11666-014-0123-0.
[13] L.-M. Berger, Hardmetals as thermal spray coatings, Powder Metall. 50 (2007) 205–214, http://dx.doi.org/10.1179/174329007X078.
[14] S. Hochstrasser(-Kurz), Y. Mueller, C. Latkoczy, S. Virtanen, P. Schmutz, Analytical characterization of the corrosion mechanisms of WC–Co by electrochemical methods and inductively coupled plasma mass spectroscopy, Corros. Sci. 49 (2007) 2002–2020, http://dx.doi.org/10.1016/j.corsci.2006.08.022.
[15] V.K. Champagne, The Cold Spray Materials Deposition Process Fundamentals and Applications, (2007) 9781845693787.
[16] B.H. Kear, R.K. Sadangi, M. Jain, R. Yao, Z. Kalman, G. Skandan, W.E. Mayo, Thermal sprayed nanostructured WC/Co hardcoatings, J. Therm. Spray Technol. 9 (2000) 399–406, http://dx.doi.org/10.1361/105996300770349863.
[17] B.S. Mann, V. Arya, HVOF coating and surface treatment for enhancing droplet erosion resistance of steam turbine blades, Wear 254 (2003) 652–667, http://dx.doi.org/10.1016/S0043-1648(03)00253-9.
[18] T. SahraouI, N.E. Feninechе, G. Montavon, C. Coddet, Structure and wear behaviour of HVOF sprayed Cr_3C_2–NiCr and WC–Co coatings, Mater. Des. 24 (2003) 309–313, http://dx.doi.org/10.1016/S0261-3069(03)00059-1.
[19] M.M. Lima, C. Godoy, P.J. Modenesi, J.C. Avelar-Batista, A. Davison, A. Matthews, Coating fracture toughness determined by Vickers indentation: an important parameter in cavitation erosion resistance of WC–Co thermally sprayed coatings, Surf. Coat. Technol. 177–178 (2004) 489–496, http://dx.doi.org/10.1016/S0257-8972(03)00917-4.
[20] B.S. Mann, V. Arya, P. Joshi, Advanced high-velocity oxygen-fuel coating and candidate materials for protecting LP steam turbine blades against droplet erosion, J. Mater. Eng. Perform. 14 (2005) 487–494, http://dx.doi.org/10.1361/105994905X56188.
[21] A.J. López, J. Rams, Protection of carbon steel against molten aluminum attack and high temperature corrosion using high velocity oxygen-fuel WC–Co coatings, Surf. Coat. Technol. 262 (2015) 123–133, http://dx.doi.org/10.1016/j.surfcoat.2014.12.023.
[22] H. Wang, X. Song, X. Wang, X. Liu, X. Wang, Fabrication of nanostructured WC–Co coating with low decarburization, Int. J. Refract. Met. Hard Mater. 53 (2015) 92–97, http://dx.doi.org/10.1016/j.ijrmhm.2015.05.010.
[23] A.S. Praveen, J. Sarangan, S. Suresh, B.H. Channabasappa, Optimization and erosion wear response of NiCrSiB/WC–Co HVOF coating using Taguchi method, Ceram. Int. 42 (2016) 1094–1104, http://dx.doi.org/10.1016/j.ceramint.2015.09.036.
[24] W. Luo, U. Selvadurai, W. Tillmann, Effect of residual stress on the wear resistance of thermal spray coatings, J. Therm. Spray Technol. 25 (2016) 321–330, http://dx.doi.org/10.1007/s11666-015-0309-0.
[25] J. Yuan, C. Ma, S. Yang, Z. Yu, H. Li, Improving the wear resistance of HVOF sprayed WC-Co coatings by adding submicron-sized WC particles at the splats' interfaces, Surf. Coat. Technol. 285 (2016) 17–23, http://dx.doi.org/10.1016/j.surfcoat.2015.11.017.
[26] M. Jafari, M.H. Enayati, M. Salehi, S.M. Nahvi, J.C. Han, C.G. Park, High temperature oxidation behavior of micro/nanostructuredWC-Co coatings deposited from Ni-coated powders using high velocity oxygen fuel spraying, Surf. Coat. Technol. 302 (2016) 426–437, http://dx.doi.org/10.1016/j.surfcoat.2016.06.044.
[27] Z. Geng, S. Hou, G. Shi, D. Duan, S. Li, Tribological behaviour at various temperatures of WC-Co coatings prepared using different thermal spraying techniques, Tribol. Int. 104 (2016) 36–44, http://dx.doi.org/10.1016/j.triboint.2016.08.025.
[28] T.C. Zhu, K. Yukimura, C.X. Ding, P.Y. Zhang, Tribological properties of nanostructured and conventional WC-Co coatings deposited by plasma spraying, Thin Solid Films 388 (2001) 277–282, http://dx.doi.org/10.1016/S0040-6090(01)00805-7.
[29] F. Ghadami, M. Heydarzadeh Sohi, S. Ghadami, Effect of TIG surface melting on structure and wear properties of air plasma-sprayed WC–Co coatings, Surf. Coat. Technol. 261 (2015) 108–113, http://dx.doi.org/10.1016/j.surfcoat.2014.11.050.
[30] F. Ghadami, M. Heydarzadeh Sohi, S. Ghadami, Effect of bond coat and post-heat treatment on the adhesion of air plasma sprayed WC-Co coatings, Surf. Coat. Technol. 261 (2015) 289–294, http://dx.doi.org/10.1016/j.surfcoat.2014.11.016.
[31] A.A. Burkov, S.A. Pyachin, Formation of WC–Co coating by a novel technique of electrospark granules deposition, Mater. Des. 80 (2015) 109–115, http://dx.doi.org/10.1016/j.matdes.2015.05.008.
[32] L. Pawlowski, The Science and Engineering of Thermal Spray Coatings, John Wiley & Sons, 9780471490494, 2008.
[33] V.G. Burov, I.A. Bataev, A.G. Tyurin, S.V. Veselov, Structure and properties of WC–Co coatings obtained on steel substrates by liquid state sintering in vacuum, Surf. Eng. 31 (2015) 540–544, http://dx.doi.org/10.1179/1743294414Y.0000000415.

[34] A.J. López, J. Rams, Protection of carbon steel against molten aluminum attack and high temperature corrosion using high velocity oxygen-fuel WC–Co coatings, Surf. Coat. Technol. 262 (2015) 123–133, http://dx.doi.org/10.1016/j.surfcoat.2014.12.023.

[35] M.S. Mahdipoor, F. Tarasi, C. Moreau, A. Dolatabadi, M. Medraj, HVOF sprayed coatings of nano-agglomerated tungsten-carbide/cobalt powders for water droplet erosion application, Wear 330–331 (2015) 338–347, http://dx.doi.org/10.1016/j.wear.2015.02.034.

[36] Z. Geng, S. Li, D.L. Duan, Y. Liu, Wear behaviour of WC–Co HVOF coatings at different temperatures in air and argon, Wear 330–331 (2015) 348–353, http://dx.doi.org/10.1016/j.wear.2015.01.035.

[37] J.M. Guilemany, S. Dosta, J. Nin, J.R. Miguel, Study of the properties of WC-Co nanostructured coatings sprayed by high-velocity oxyfuel, J. Therm. Spray Technol. 14 (2005) 405–413, http://dx.doi.org/10.1361/105996305X59350.

[38] J.M. Guilemany, S. Dosta, J.R. Miguel, The enhancement of the properties of WC-CoHVOF coatings through the use of nanostructured and microstructured feedstock powders, Surf. Coat. Technol. 201 (2006) 1180–1190, http://dx.doi.org/10.1016/j.surfcoat.2006.01.041.

[39] S. Dosta, J.R. Miguel, J.M. Guilemany, Nanostructured cermet coatings with enhanced properties produced by HVOF thermal spray, Mater. Sci. Forum 587–588 (2008) 1024–1028, http://dx.doi.org/10.4028/www.scientific.net/MSF.587-588.1024.

[40] M. Li, P.D. Christofides, Modeling and control of high-velocity oxygen-fuel (HVOF) thermal spray: a tutorial review, J. Therm. Spray Technol. 18 (2009) 753–768, http://dx.doi.org/10.1007/s11666-009-9309-2.

[41] A. Lekatou, D. Zois, D. Grimanelis, Corrosion properties of HVOF cermet coatings with bond coats in an aqueous chloride environment, Thin Solid Films 516 (2008) 5700–5705, http://dx.doi.org/10.1016/j.tsf.2007.07.130.

[42] M. Magnani, P.H. Suegama, N. Espallargas, C.S. Fugivara, S. Dosta, J.M. Guilemany, a.V. Benedetti, Corrosion and wear studies of Cr3C2NiCr-HVOF coatings sprayed on AA7050 T7 under cooling, J. Therm. Spray Technol. 18 (2009) 353–363, http://dx.doi.org/10.1007/s11666-009-9305-6.

[43] Y. Wang, S.L. Jiang, Y.G. Zheng, W. Ke, W.H. Sun, J.Q. Wang, Effect of porosity sealing treatments on the corrosion resistance of high-velocity oxy-fuel (HVOF)-sprayed Fe-based amorphous metallic coatings, Surf. Coat. Technol. 206 (2011) 1307–1318, http://dx.doi.org/10.1016/j.surfcoat.2011.08.045.

[44] G.-C. Ji, H.-T. Wang, X. Chen, X.-B. Bai, Z.-X. Dong, F.-G. Yang, Characterization of cold-sprayed multimodal WC-12Co coating, Surf. Coat. Technol. 235 (2013) 536–543, http://dx.doi.org/10.1016/j.surfcoat.2013.08.021.

[45] H.J. Kim, C.H. Lee, S.Y. Hwang, Fabrication of WC-Co coatings by cold spray deposition, Surf. Coat. Technol. 191 (2005) 335–340, http://dx.doi.org/10.1016/j.surfcoat.2004.04.058.

[46] N. Bala, H. Singh, J. Karthikeyan, S. Prakash, Cold spray coating process for corrosion protection: a review, Surf. Eng. 30 (2014) 414–421, http://dx.doi.org/10.1179/1743294413Y.0000000148.

[47] S. Dosta, G. Bolelli, A. Candeli, L. Lusvarghi, I.G. Cano, J.M. Guilemany, Plastic deformation phenomena during cold spray impact of WC-Co particles onto metal substrates, Acta Mater. 124 (2017) 173–181, http://dx.doi.org/10.1016/j.actamat.2016.11.010.

[48] A. Moridi, S.M. Hassani-Gangaraj, M. Guagliano, M. Dao, Cold spray coating: review of material systems and future perspectives, Surf. Eng. 30 (2014) 369–395, http://dx.doi.org/10.1179/1743294414Y.0000000270.

[49] B. Jodoin, L. Ajdelsztajn, E. Sansoucy, A. Zúñiga, P. Richer, E.J. Lavernia, Effect of particle size, morphology, and hardness on cold gas dynamic sprayed aluminum alloy coatings, Surf. Coat. Technol. 201 (2006) 3422–3429, http://dx.doi.org/10.1016/j.surfcoat.2006.07.232.

[50] P.H. Gao, C.J. Li, G.J. Yang, Y.G. Li, C.X. Li, Influence of substrate hardness on deposition behavior of single porous WC-12Co particle in cold spraying, Surf. Coat. Technol. 203 (2008) 384–390, http://dx.doi.org/10.1016/j.surfcoat.2008.09.016.

[51] Z. Zhao, G.S. Frankel, On the first breakdown in AA7075-T6, Corros. Sci. 49 (2007) 3064–3088, http://dx.doi.org/10.1016/j.corsci.2007.02.001.

[52] Z. Zhao, G.S. Frankel, The effect of temper on the first breakdown in AA7075, Corros. Sci. 49 (2007) 3089–3111, http://dx.doi.org/10.1016/j.corsci.2007.02.004.

[53] W.S. TAIT, An Introduction to Electrochemical Corrosion Testing for Practicing Engineers and Scientists, Pair Odocs, Wisconsin, 1994.

[54] K. Balani, T. Laha, A. Agarwal, J. Karthikeyan, N. Munroe, Effect of carrier gases on microstructural and electrochemical behavior of cold-sprayed 1100 aluminum coating, Surf. Coat. Technol. 195 (2005) 272–279, http://dx.doi.org/10.1016/j.surfcoat.2004.06.028.

[55] M.M. Sharma, T.J. Eden, B.T. Golesich, Effect of surface preparation on the microstructure, adhesion, and tensile properties of cold-sprayed aluminum coatings on AA2024 substrates, J. Therm. Spray Technol. 24 (2014) 410–422, http://dx.doi.org/10.1007/s11666-014-0175-1.

[56] X. Zhou, P. Mohanty, Electrochemical behavior of cold sprayed hydroxyapatite/titanium composite in Hanks' solution, Electrochim. Acta 65 (2012) 134–140, http://dx.doi.org/10.1016/j.electacta.2012.01.018.

[57] N.M. Melendez, A.G. McDonald, Development of WC-based metal matrix composite coatings using low-pressure cold gas dynamic spraying, Surf. Coat. Technol. 214 (2013) 101–109, http://dx.doi.org/10.1016/j.surfcoat.2012.11.010.

[58] K. Spencer, M.X. Zhang, Heat treatment of cold spray coatings to form protective intermetallic layers, Scr. Mater. 61 (2009) 44–47, http://dx.doi.org/10.1016/j.scriptamat.2009.03.002.

[59] K. Spencer, D.M. Fabijanic, M.X. Zhang, The use of Al-Al2O3 cold spray coatings to improve the surface properties of magnesium alloys, Surf. Coat. Technol. 204 (2009) 336–344, http://dx.doi.org/10.1016/j.surfcoat.2009.07.032.

[60] E. Zalnezhad, Ahmed A.D. Sarhan, M. Hamdi, Investigating the effects of hard anodizing parameters on surface hardness of hard anodized aerospace AL7075-T6 alloy using fuzzy logic approach for fretting fatigue application, Int. J. Adv. Manuf. Technol. 68 (2013) 453–464, http://dx.doi.org/10.1007/s00170-013-4743-1.

[61] B. Venkataraman, G. Sundararajan, Correlation between the characteristics of the mechanically mixed layer and wear behaviour of aluminium, Al-7075 alloy and Al-MMCs, Wear 245 (2000) 22–38, http://dx.doi.org/10.1016/S0043-1648(00)00463-4.

[62] X.T. Luo, C.X. Li, F.L. Shang, G.J. Yang, Y.Y. Wang, C.J. Li, WC-Co composite coating deposited by cold spraying of a core-shell-structured WC-Co powder, J. Therm. Spray Technol. 24 (2014) 100–107, http://dx.doi.org/10.1007/s11666-014-0133-y.

[63] S. Maitra, G.C. English, Mechanism of localized corrosion of 7075 alloy plate, Metall. Trans. (1981) 535–541, http://dx.doi.org/10.1007/BF02648553.

[64] U. Tiringer, J. Kovac, I. Milosev, Effects of mechanical and chemical pre-treatments on the morphology and composition of surfaces of aluminium alloys 7075-T6 and 2024-T3, Corros. Sci. 119 (2017) 46–59, http://dx.doi.org/10.1016/j.corsci.2017.02.018.

[65] S. Lameche-Djeghaba, A. Benchettara, F. Kellou, V. Ji, Electrochemical behaviour of pure aluminium and Al–5%Zn alloy in 3% NaCl solution, Arab. J. Sci. Eng. 39 (2013) 113–122, http://dx.doi.org/10.1007/s13369-013-0876-7.

[66] A.B. Oliveira, A.C. Bastos, C.M. Fernandes, C.M.S. Pinho, A.M.R. Senos, E. Soares, J. Sacramento, M.L. Zheludkevich, M.G.S. Ferreira, Corrosion behaviour of WC-10% AISI 304 cemented carbides, Corros. Sci. 100 (2015) 322–331, http://dx.doi.org/10.1016/j.corsci.2015.08.006.

[67] S. Hochstrasser-Kurz, D. Reiss, T. Suter, C. Latkoczy, D. Günther, S. Virtanen, P.J. Uggowitzer, P. Schmutz, ICP-MS, X.P.S. SKPFM, and Microcapillary, Investigation of the local corrosion mechanisms of WC–Co hardmetal, J. Electrochem. Soc. 155 (2008) C415–C426, http://dx.doi.org/10.1149/1.2929822.

[68] A.M. Human, H.E. Exner, Electrochemical behaviour of tungsten-carbide hardmetals, Mater. Sci. Eng. A 209 (1996) 180–191, http://dx.doi.org/10.1016/0921-5093(95)10137-3.

[69] Y. Liu, A. Laurino, T. Hashimoto, X. Zhou, P. Skeldon, G.E. Thompson, G.M. Scamans, C. Blanc, W.M. Rainforth, M.F. Frolish, Corrosion behaviour of mechanically polished AA7075-T6 aluminium alloy, Surf. Interface Anal. 42 (2010) 185–188, http://dx.doi.org/10.1002/sia.3136.

[70] N. Schubert, M. Schneider, A. Michealis, The mechanism of anodic dissolution of cobalt in neutral and alkaline electrolyte at high current density, Electrochim. Acta 113 (2013) 748–754, http://dx.doi.org/10.1016/j.electacta.2013.06.093.

[71] W.J. Tomlinson, C.R. Linzell, Anodic polarization and corrosion of cemented carbides with cobalt and nickel binders, J. Mater. Sci. 23 (1988) 914–918, http://dx.doi.org/10.1007/BF01153988.

[72] O. Meydanoglu, B. Jodoin, E.S. Kayali, Microstructure, mechanical properties and corrosion performance of 7075 Al matrix ceramic particle reinforced composite coatings produced by the cold gas dynamic spraying process, Surf. Coat. Technol. 235 (2013) 108–116, http://dx.doi.org/10.1016/j.surfcoat.2013.07.020.

[73] W.A. Badawy, F.M. Al-Kharafi, J.R. Al-Ajmi, Electrochemical behavior of cobalt in aqueous solutions of different pH, J. Appl. Electrochem. 30 (2000) 693–704, http://dx.doi.org/10.1023/A:100389312.

[74] M.E. Orazem, B. Tribollet, Electrochemical Impedance Spectroscopy, ECS-The Electrochemical Society, Pennington, NJ, 2008.

[75] N.M. Chavan, B. Kiran, A. Jyothirmayi, P.S. Phani, G. Sundararajan, The corrosion behavior of cold sprayed zinc coatings on mild steel substrate, J. Therm. Spray Technol 22 (2013) 463–470, http://dx.doi.org/10.1007/s11666-013-9893-z.